Original Article



Retrieval of Phase Information from Low-Dose Electron Microscopy Experiments: Are We at the Limit Yet?

Francisco Vega Ibáñez^{1,2}, and Jo Verbeeck^{1,2,*}

- ¹EMAT, University of Antwerp, Groenenborgerlaan 171 2020, Antwerp, Belgium
- ²Nanocenter of excellence, University of Antwerp, Groenenborgerlaan 171 2020, Antwerp, Belgium

Abstract

The challenge of imaging low-density objects in an electron microscope without causing beam damage is significant in modern transmission electron microscopy. This is especially true for life science imaging, where the sample, rather than the instrument, still determines the resolution limit. Here, we explore whether we have to accept this or can progress further in this area. To do this, we use numerical simulations to see how much information we can obtain from a weak phase object at different electron doses. Starting from a model with four phase values, we compare Zernike phase contrast with measuring diffracted intensity under multiple random phase illuminations to solve the inverse problem. Our simulations have shown that diffraction-based methods perform better than the Zernike method, as we have found and addressed a normalization issue that, in some other studies, led to an overly optimistic representation of the Zernike setup. We further validated this using more realistic 2D objects and found that random phase illuminated diffraction can be up to five times more efficient than an ideal Zernike implementation. These findings suggest that diffraction-based methods could be a promising approach for imaging beamsensitive materials and that current low-dose imaging methods are not yet at the quantum limit.

Key words: inverse problem, multiplex holography, phase plates, phase retrieval, ptychography, Zernike phase contrast

Introduction

In this work, we aim to revisit the longstanding issue of phase reconstruction in transmission electron microscopy (TEM) (Drenth et al., 1975; Fienup, 1982; Coene et al., 1992; McCallum & Rodenburg, 1992, 1993; Rodenburg et al., 1993) and examine it from the perspective of information transfer. In electron microscopy, we detect electron events that are quantum-mechanically linked to their wavefronts' probability density (square modulus). The problem arises from the loss of the phase during the detection process, which significantly restricts the information obtainable from an electron microscope experiment. This issue is particularly challenging in electron diffraction experiments, as it hinders the extraction of the projected periodic potential of a crystal. Moreover, it is also highly relevant in imaging non-periodic thin objects in TEM, where the object's projected density information is predominantly encoded in the phase profile imparted on the coherent plane wave illumination. Recent attempts to apply diffraction-based imaging, e.g., to viruses (Zhou et al., 2020) or in single particle analysis (Pei et al., 2023) show great potential and are accompanied by promising simulation studies (Pelz et al., 2017; Leidl et al., 2023; Mao et al., 2024).

We will use the toolset of parameter estimation, which has shed light on similar problems in TEM, like investigating point resolution in the presence of noise (Bettens et al., 1999), the advantage of a monochromator on the spatial resolution in TEM (den Dekker et al., 2001), determining the precision of measuring atomic positions from exit waves (De Backer et al., 2011), or even determining elemental concentrations

from electron energy loss experiments (Verbeeck, 2024; Verbeeck & Van Aert, 2004). The issue of phase retrieval under dose-limited conditions has sparked significant debate within the scientific community. Egerton et al. conducted groundbreaking research to assess the instrument's limitations (Egerton, 2007) and evaluated different commonly used TEM and scanning transmission electron microscopy (STEM) imaging methods on beam-sensitive specimens (Egerton, 2013). In the following years, more theory was incorporated to assess the efficiency of phase retrieval by incorporating robust mathematical concepts such as the Fischer Information (FI) and Cramér-Rao Lower Bound (CRLB) (Bouchet et al., 2021). Based on these mathematical concepts, Koppell & Kasevich (2021) constructed a function to assess the inherent frequency transfer of the imaging system. More recently, Dwyer and Paganin directly compared Zernike Phase Contrast (ZPC) and 4D-STEM with a phase-structured illumination. All this notable work has paved the way and opened the debate for a more comprehensive assessment of phase retrieval in the TEM, with the general conclusion that ZPC seemed the best method to maximize information transfer. Ultimately, this conclusion has put limits on the hope for ptychographic methods to create a breakthrough in low-dose phase imaging (Fienup, 1982; Nellist et al., 1995; Faulkner & Rodenburg, 2004; Maiden & Rodenburg, 2009; Parvizi et al., 2015; Yang et al., 2015). Here, we revisit this problem by conducting a series of numerical exercises. Furthermore, we will carefully consider the normalization conditions to enable a fair comparison between image-based reconstruction using ZPC and phase retrieval through diffraction-based recording. We

^{*}Corresponding author: Jo Verbeeck, E-mail: jo.verbeeck@uantwerpen.be

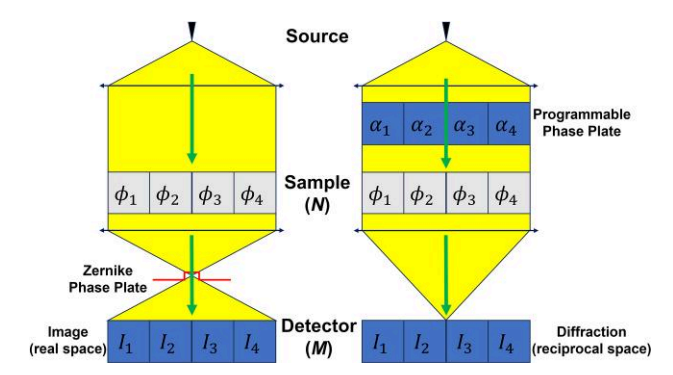


Fig. 1. Sketch of the setup. The aim is to measure the *N* phases of the unknown object by illuminating it with a coherent electron wave and detecting the arrival of electrons with an ideal detector consisting of *M* independent pixels. The left-side setup shows the configuration with an ideal ZPP, while the right-side setup describes the detection in the diffraction plane with a programmable phase input wave. We will compare the performance of both setups in terms of phase error on the estimate as a function of the amount of electrons we have available in the experiment.

demonstrate that at least under the idealized conditions considered here, significant improvement over ZPC in low-dose phase imaging is possible with diffraction-based detection.

Setup

In the following section, we want to present this process as a type of *game* where the sample is imagined to contain a hidden message made up of N phase values, denoted as ϕ_i in Figure 1. We illuminate the sample with an electron wave and observe the outcome of this interaction on M ideal electron detectors, labeled as I_i in Figure 1. From this simple setup, two natural questions arise:

- How many electrons do we need to fire onto the sample to obtain the secret message at the required precision and accuracy?
- How can the experiment be set up to achieve the best precision and accuracy with the fewest electrons and, thus, the least beam damage?

These questions are fundamental in modern electron microscopy, as the resolution of EM is in many practical cases limited by beam damage and not anymore by the instrument (Glaeser, 1971; Chen et al., 2008; Müller-Caspary et al., 2019; Nakane et al., 2020; Chari & Stark, 2023; Pei et al., 2023; Küçükoğlu et al., 2024; Leidl et al., 2024). This means we must either learn new techniques to limit beam damage or utilize the most efficient imaging methods to maximize the use of the electron dose the sample can withstand (preferably a combination of both).

In this paper, we will avoid all complications regarding the scattering that happens with the sample, details of imperfect optical systems (Gonsalves, 1982; Fienup, 1993), propagation effects (Liu et al., 2009; Robert et al., 2022), multiple scattering in the sample (Maiden et al., 2012; Chen et al., 2020, 2024; Ren et al., 2020), inelastic scattering (Yoshioka, 1957; Muller & Silcox, 1995; Dwyer, 2005; Dwyer et al., 2008; Allen et al., 2015; Brown et al., 2018; Beyer et al., 2020; Robert et al., 2022; Diederichs et al., 2024), partial coherence (Nellist & Rodenburg, 1994; Gureyev et al., 2006; Martin et al., 2006; Thibault & Menzel, 2013; Oxley

& Dyck, 2020; Diederichs et al., 2024), and details of the algorithmic implementation (Fannjiang & Liao, 2012; Elser et al., 2018) to gain some clarity on how far we are from fundamental limits.

We start with a conceptual exercise to estimate four hidden phases as sketched in Figure 1. We compare two typical setups: On the one hand, we use a Zernike Phase Plate (ZPP) for phase contrast imaging, which is commonly considered the golden standard in real space phase imaging and is used extensively in, e.g., life science imaging (Zernike, 1942a, 1942b; Danev & Nagayama, 2001, 2008). The benefit of this method is that it results directly in an image of the sample with a contrast that relates approximately linearly to the phase shift, which is proportional to the projected electrostatic potential of the thin sample in a TEM.

On the other hand, we can detect the scattered electrons in the diffraction plane as is commonly done to investigate symmetries and periodicity in crystals. This pattern also encodes the information of the specimen albeit in a different way and requiring some inverse algorithm to link the recorded intensities to the projected sample potential we are interested in.

In either case, retrieving the *absolute phase* will be impossible as we have no unperturbed reference beam to compare. Due to this lack of a reference beam, only three of the four unknown phases are independent, somewhat simplifying the problem from N to (N-1) unknowns represented as $\phi_N = -\sum_1^{N-1} \phi_i$.

Because either a translation or an inversion of the object leaves the diffraction intensities unchanged, we have a good chance of ending up with a wrong guess of the secret sample for the diffraction-based setup (Guizar-Sicairos & Fienup, 2012; Tolimieri et al., 2012). A typical way to solve this is to oversample the diffraction plane (M > N), which stabilizes the solution at the expense of requiring more detector pixels. Another way to proceed is by introducing an amplitude (Allars et al., 2021; Abregana & Almoro, 2022; You et al., 2023) or phase (Verbeeck et al., 2018; Vega Ibáñez et al., 2023; Yu et al., 2023) modulator capable of encoding the electron wavefront for $N_{\text{config.}}$ sets of conditions. Here, we focus on pure phase modulation without delving into the details of how to create such a programmable phase modulator (Vega Ibáñez et al., 2023; Yu et al., 2023) and simply assume it to be perfect, as we did for ZPC.

Suppose we choose a number of Random Phase Illumination (RPI) conditions $N_{\rm RPI}$, and we solve the inverse problem by taking into account the $N_{\rm RPI}$ independent measurements to resolve one unique estimate of the object phase. We now obtain some robustness against inversion and translation since the extra configurations yield $M \times N_{\rm RPI}$ measurement points (far more than the N unknown phases we want to recover).

In order to implement this scheme, we use a nonlinear maximum-likelihood (ML) fitting algorithm with (N-1) unknown phases and a likelihood function assuming Poisson counting noise that describes how likely it is that a given experimental realization of $M \times N_{\rm RPI}$ diffraction intensities could have been produced when assuming a given set of (N-1) sample phases (Cramer, 1946; Barlow, 1991). This iterative nonlinear fitting process is significantly slower than the more common Gerchberg–Saxton (GS) (Gerchberg, 1972) algorithm but allows the correct treatment of the Poisson statistics and obtaining estimates for the connection between phase errors and the counting statistics through the use of the

Cramér–Rao lower bound (Rao, 1945; Cramer, 1946). We can then use this to compare the behavior of the GS algorithm to ML prediction to convince ourselves that it approaches the same fundamental limit while providing a significant speed-up needed for realistic image sizes.

Recovering the Phase and Estimating its Precision

Our objective is to accurately determine the unknown phase from either a real-space or diffraction-space intensity recording. We will use the ZPC method for real space as a standard, and in the case of the diffraction experiment, we will need to solve the inversion problem. To do so, we will utilize parameter estimation to understand its statistical properties and, later, use a GS algorithm that can approach these while providing a significant numerical speed advantage.

Zernike Phase Contrast

In ZPC (Zernike, 1942*a*, 1942*b*), a phase plate is placed in the back focal plane of the objective aperture, which shifts only the low-frequency component of the wave by $\pi/2$. As a result, the image contrast now reveals the phase of the object. In Appendix A, we derive the relationship between phase and image contrast, paying attention to proper normalization (see equation (A.17)). This aspect has remained under-illuminated but will be critically important when studying the effect of counting noise:

$$\phi(\mathbf{r}) = \frac{I_z(\mathbf{r}) - 1 + 2C^2 - 2C^4}{2C^2}.$$
 (1)

With I_Z , the recorded intensity scaled such that if the ZPP were removed, there would be an average of 1 electron per pixel. The factor $C = Rk_Z$ is given as the radius of the illumination disc R on the sample times the size of the central phase shifting area k_Z in reciprocal units, and the formula is valid only for $C \le 1/2$ as we will lose low-frequency information for higher values of C. In the derivation, we assumed a Heavyside pi function for the phase profile, which gives the most faithful phase recovery (but may be harder to achieve in practice). The critical thing to note here is that this formula only agrees with the conventional ZPC for C = 1. However, in this case, the formula is not valid, as important low-frequency information would be missing across the illuminated area because the reference wave generated by the central Zernike phase discontinuity would not be homogeneous. Only if we admit to being interested in a subregion of the illuminated area can we recover the conventional formula at C = 1. It is important to stress here that, in such a case, we create a situation that cannot longer act as a fair comparison with the diffraction setup for the following reasons:

- We are illuminating and damaging areas of the sample outside the field of view. We might need those areas later on.
- We use electrons outside the field of view which will help to create a reference beam inside the field of view. This effectively creates a setup similar to an off-axis holography experiment (Lichte & Lehmann, 2007) and results in an unfair counting of the incoming amount of electrons that is needed per area. If such an external reference wave can be added at no penalty, then this option should also be offered to the diffraction setup, e.g., by assuming

- that part of the illuminated field of view is known to be constant or of no interest. This would lower the amount of unknowns and increase the precision as well.
- Even if the area of the sample around the region of interest can be considered uninteresting or sacrificial, the electrons hitting there can still cause damage inside the area of interest via delocalized inelastic scattering (Egerton, 2012, 2017; Jannis et al., 2022; Velazco et al., 2022)

In order to recover all spatial frequencies within the illuminated area without creating an (unfair) implicit reference wave, we choose to take the optimal value of C = 1/2 for the remainder of this work. With that normalization in mind, we can estimate the standard deviation of the phase error for N_e electrons as:

$$\sigma_{\phi,Z,2D} = \frac{\sqrt{1 - 2C^2 + 2C^4}}{2C^2\sqrt{N_e/(N-1)}} \stackrel{C=1/2}{\longrightarrow} \frac{\sqrt{10}}{2\sqrt{N_e/(N-1)}},$$
 (2)

which is $\sqrt{10} \approx 3.16$ times *higher* than what we would get assuming the wrongly normalized conventional solution. Note that, for a 1D case, the normalization penalty is less severe:

$$\sigma_{\phi,Z,1D} = \frac{\sqrt{1 - 2C + 2C^2}}{2C^2\sqrt{N_e/(N - 1)}} \stackrel{C=1/2}{\to} \frac{\sqrt{2}}{2\sqrt{N_e/(N - 1)}}.$$
 (3)

To make matters more confusing, it turns out that when numerically implementing ZPC, this aliasing error is often made by wrongly assuming that illumination and sample are periodically repeated until infinity, resulting in a situation that exactly replicates the C=1 case without even having the penalty of losing the low-frequency information. This subtle error that we discuss in more detail in Appendix B is likely why, in other numerical attempts, the counting noise effect is portrayed too optimistically (Koppell & Kasevich, 2021; Dwyer, 2023). To help overcome this situation, we include a numerical reference implementation with this paper (Verbeeck & Vega, 2024).

Inversion via Parameter Estimation

Estimating the parameters of a forward model is a simple method for determining the unknown phases from a recorded diffraction pattern (Aster et al., 2018). We can model the object as a discrete pure-phase object:

$$S_i = e^{i\phi_i}. (4)$$

Then, we can describe the illumination over this object with a wave function:

$$\Psi_i = A_i e^{i\alpha_i}. (5)$$

To allow for both amplitude and phase modulation, we can write the exit wave of the object as:

$$\Psi_i = A_i e^{i(\phi_i + \alpha_i)}. \tag{6}$$

Moreover, we record the diffraction intensities as follows:

$$I_{\text{model},i} = |\mathcal{F}_i \Psi_i|^2. \tag{7}$$

With \mathcal{F}_j representing the Fourier transform operator, which projects the wave onto the back focal plane where the detection process occurs. Now, we can define a maximum-likelihood estimator (MLE) based on the assumption that the detection in the diffraction plane is governed by counting

noise, and each detector pixel is assumed to be independent. We can write the log-likelihood l (Van den Bos, 1989) as:

$$l \approx -\sum_{j} (I_{\exp,j} \ln (I_{\text{model},j}) - I_{\text{model},j}).$$
 (8)

With $I_{\exp,j}$ and $I_{\text{model},j}$, the experimental and model intensities, respectively. We can now use a nonlinear fitting algorithm to find the estimates $\tilde{\phi}_i$ of ϕ_i . The ML algorithm has the benefit of delivering estimates with the highest possible precision and without bias for a high number of observations (Den Dekker et al., 2005), assuming the model and the noise model are correct. In Appendix C, we derive the Jacobian for this model, which significantly speeds up the iterative optimization routine. Furthermore, we also do the derivation for the Fisher information matrix, which can be inverted to obtain the Cramér–Rao Lower Bound (CRLB) (Den Dekker et al., 2005).

$$\sigma_{\phi, \text{ML}} \ge \text{CRLB} = \sqrt{\frac{\text{Tr}(F^{-1})}{N-1}}$$
 (9)

With Tr(), the Trace operator, and *F*, the Fisher information matrix. We can further estimate the CRLB from a more fundamental perspective. We detect in the reciprocal plane where, in principle, information related to the phase of the object is encoded in both amplitude and phase in that plane. As a result, we can, at best, obtain an average of half of the information, as we have assumed no prior information about the object. We could, therefore, assume that the CRLB will be close to the following:

$$CRLB \approx \frac{\sqrt{2}}{2\sqrt{N_e/(N-1)}}$$
 (10)

This was given as well in equation (3) as the correction for the 1D case in a ZPC system with C = 1/2. However, we will numerically test this idea further on.

The CRLB can predict the best possible precision that can be obtained under the given electron dose. This can then be compared to the actual outcome of a numerical experiment to evaluate whether we can attain the CRLB in practice. It can also serve to compare alternative algorithms like GS to evaluate how close this can approach this limit and check if bias is introduced.

Inversion via the Gerchberg-Saxton algorithm

The GS algorithm and its variations are iterative methods used to recover phase information from intensity measurements of a complex-valued wave function (Gerchberg, 1972; Yang et al., 1994; Zalevsky et al., 1996; Huang et al., 2020). In our case, starting from a set of intensity recordings in diffraction space $\hat{I} = \{I_1, I_2, \ldots, I_{N_{RPI}}\}$, and their corresponding known illumination patterns in real space $\hat{\Psi} = \{\Psi_1, \Psi_2, \ldots, \Psi_{N_{RPI}}\}$, we aim to retrieve the (N-1) missing phases of an object \hat{S} . To do this, we can start by guessing our solution \hat{S}_0^* as a set of N complex numbers with amplitude 1 and random phases $\phi_i \in [-\pi, \pi)$, illuminated by the complex-valued waves from each N_{RPI} measurement in diffraction space. And, in general, for any given iteration:

$$\hat{\varphi}_{\text{out},i}^{\star} = \mathcal{F}[\hat{S}_{i}^{\star}\hat{\Psi}]. \tag{11}$$

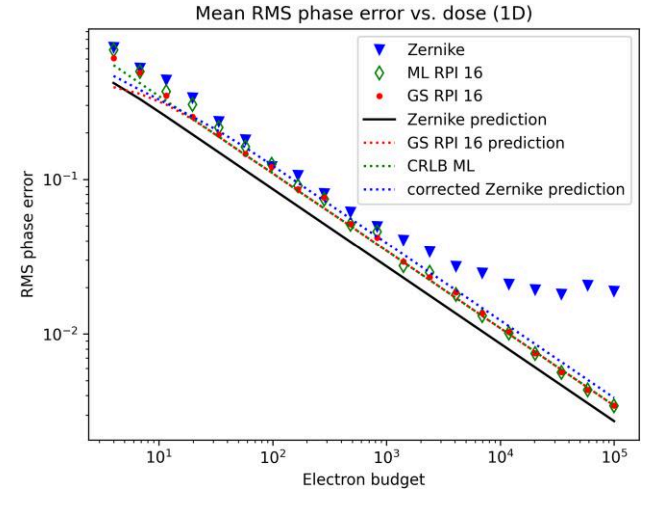


Fig. 2. Numerical simulation of the average RMS phase error as a function of total electron dose. The object is considered a random phase object with four unknown phase values and a limited phase range of $\pm \pi/10$ to stay within the linear approximation of the ZPC formula. The simulation is repeated 100 times for each electron budget with a different random object. Random phase illumination is done with 16 random illumination patterns that stay the same throughout the simulation set. Note how ZPC and RPI's results closely follow the predicted statistical error and show a similar noise performance up to about $N_e = 10^4$, where systematic errors due to the linearization of the ZPC formula start to show. Note also how ML RPI and GS RPI perform remarkably similarly, giving confidence in the GS approach for larger systems.

From this, we can impose the constraint of our recording in diffraction space and re-construct our guessed $\hat{\varphi}_{\text{out } i+1}^{\star}$ as:

$$\hat{\varphi}_{\text{out},i+1}^{\star} = \frac{\hat{\varphi}_{\text{out},i}^{\star}}{\|\hat{\varphi}_{\text{out},i}^{\star}\|} \sqrt{\hat{I}} \times \text{Phase}(\hat{\varphi}_{\text{out},i}^{\star}), \tag{12}$$

where the Phase operator returns the phase of the given array, respectively. From this, we can back-propagate $\hat{\varphi}_{\text{out},i+1}^{\star}$ to real space and obtain a new estimate for the object:

$$\hat{S}_{i+1}^{\star} = \text{Average}\left(\mathcal{F}^{-1}[\hat{\varphi}_{\text{out},i+1}^{\star}]\hat{\Psi}_{in}^{\dagger}\right). \tag{13}$$

With $\hat{\Psi}_{in}^{\dagger}$ being the complex conjugate of the transposed illumination pattern wave set. This process is then carried out iteratively until a set number of iterations or a convergence condition is met.

It is important to note that in equation (13), the update takes the average update from each of the $N_{\rm RPI}$ illuminating patterns. This helps reduce the typical twin and translational artifacts in the Fourier transform when $N_{\rm RPI} > 1$. For $N_{\rm RPI} = 1$, we will encounter a similar problem to that of ZPC, where oversampling is needed to solve all N phase values in our object.

Numerical Exercise for 4 Unknown Phases (1D)

An example of an outcome of this numerical experiment is given in Figure 2 for $N_{\rm RPI} = 16$. We note a logarithmic behavior between phase errors as a function of the total number of electrons (as expected). Furthermore, for this 1D case, both RPI and ZPC perform similarly. This performance shows that the corrected error prediction for ZPC in equation (3) describes the propagation of the counting noise to the estimated

phase quite well. For very high doses (above $N_e = 10^4$ here), the ZPC phase error does not decrease anymore; this is due to hitting the limit of the linearization of the ZPC formula (equation (A.16)), which also depends on the range of phase modulation δ by the sample (here $\pm \pi/10$). We are, however, more interested in the low-dose performance. Both the ML and GS results are well predicted by the CRLB, showing that, on average, we approach the statistical limit for 100 repeated experiments per electron dose value. It also shows that our rough estimate in equation (10) is reasonably accurate (in this case, it coincides with the ZPC corrected prediction) albeit slightly higher than the actual CRLB that is based on the detailed model. The fact that GS attains the CRLB also gives confidence in this much faster algorithm, which will be needed for larger systems later. We investigated the role of N_{RPI} in the number of random phase illuminations (not shown) and observed that from $N_{RPI} \ge 2$, we converge to the optimal phase error. This convergence confirms the theoretical prediction in (Fannjiang & Liao, 2012). Increasing N_{RPI} leads only to faster convergence, which might benefit larger systems. However, from here on, we will assume $N_{RPI} = 16$ unless otherwise noted. Furthermore, we found that convergence is best for random phases from a uniform distribution between 0 and π . However, other phase modulation ranges for the illumination were tested with similar results, provided that the object's phase range is fixed. Other phase patterns were attempted, such as illuminating with only 1 pixel at a random phase between $-\pi/2$ and $+\pi/2$ for each RPI configuration or using an orthogonal set of waves (e.g., a Hadamard (1893) basis set), both of which also yielded good results.

Numerical Exercise for a Small 2D Case

Changing to a more common 2D configuration, we attempt a 4 × 4 pixel phase object shown in Figure 3. The diffraction-based recording performs better than the corrected ZPC intensity, increasing dose efficiency by 5. Comparing ML RPI with GS RPI shows that GS attains the CRLB rather well, which gives faith in the algorithm as a faster alternative to ML, allowing for reconstructing larger objects in a reasonable time. The higher number of unknowns also stabilizes the statistical errors, and the observed behavior for 100 random weak phase object realizations results in an average behavior that closely follows the CRLB and ZPC error predictions. In this case, we barely start appreciating the systematic linearization error for the ZPC setup as the overall error has increased due to the higher number of unknowns, which shifts this point to higher doses.

A More Realistic 2D Object

Due to computational limitations, we have decided to use the GS algorithm for larger objects. As observed in previous examples the GS algorithm closely approximates the ML CRLB, in agreement with, e.g., Melnyk (2023). In Figure 4, we display the observed Root Mean Squared (RMS) phase error for a 64×64 random phase object with a $\pm \pi/10$ phase variation. Both methods effectively retrieve the object at high electron doses, but the standard deviation of the phase error remains about $\sqrt{5}$ higher for the correctly sampled ZPC case. We observe a similar systematic error when $N_e \geq 10^7$, which is expected at higher doses compared to the N=4 1D case. This is because we have to estimate approximately 1,000 times more phases, so the error

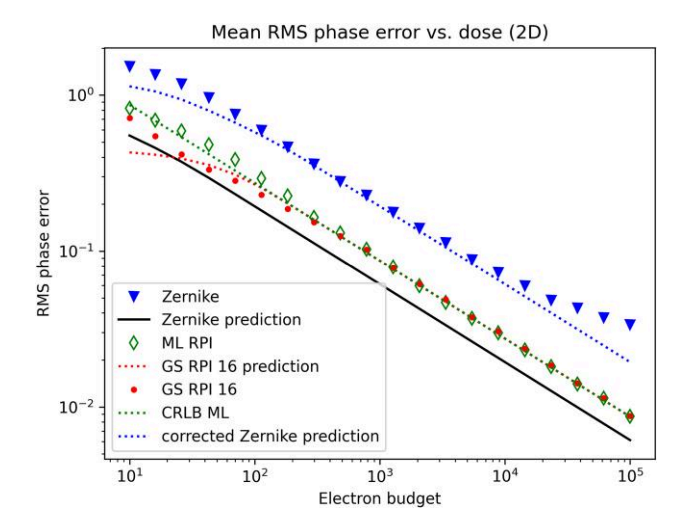


Fig. 3. Numerical simulation of a 4×4 phase object encoding 100 different realizations of random phase noise with a range of $\pm \pi/10$ for each electron budget. The electron budget is divided over 16 random phase illumination patterns. Note the significant difference with ZPC due to the normalization correction and the close relation between the ML RPI and the much faster GS RPI.

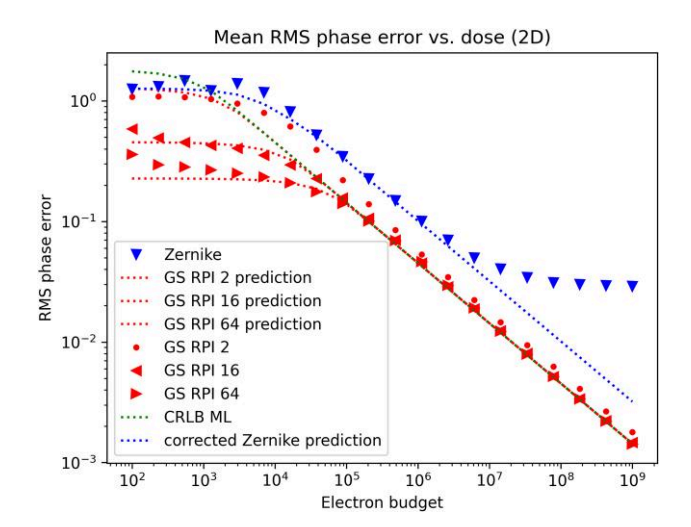


Fig. 4. RMS phase error for a single 64×64 random phase object with $\pi/10$ phase range, illuminated with $N_{\rm RPI} = 2$, 16, 64. We note that ZPC and GS closely follow their predicted error behavior as a function of the total dose. We note a remarkable trend at low doses where the phase error shows a plateau depending on $N_{\rm RPI}$, which is a consequence of phase wrapping in the individual $N_{\rm RPI}$ realizations.

requires a dose 1,000 times higher to have the same phase error in each pixel. On the low-dose end, we note a peculiar deviation from the error prediction for both ZPC and GS. This occurs because, in both cases, the phase error is bounded. For ZPC, this occurs, e.g., when we get zero counts in a pixel. In that case, the phase is fixed at $\phi_i = -10/8$ rad (for 2D), as is obvious from equation (1). Suppose we now calculate the standard deviation of a distribution which is a truncated normal distribution. In that case, we get an RMS value lower than expected from noise considerations only. This leads to a plateau at a very low dose. Note that this plateau does not mean we gained anything regarding information retrieval but is merely an effect of truncation. This effect is clearly visible in a ZPC image of the famous cameraman (Unknown, 1978) (see the top rows of

Fig. 5). When using the lowest dose, most pixels are stuck at the lowest value (-10/8) for the ZPC case), resulting in a low-phase error for an object with limited phase variation. However, these pixels do not contain much information about the object either.

The situation is more complex for the RPI measurements. For a GS implementation, we can think of RPI as a series of N_{RPI} individual measurements. Each of these measurements will have only a fraction of the total dose and, therefore, show a higher error individually. The truncation described above now happens for each realization individually, leading to a phase error plateau lower by $\sqrt{N_{\rm RPI}}$ for the low-dose cases. Naturally, this does not happen for the ML implementation because there is only one model with N phases that are bound between $-\pi$ and $+\pi$, and the $N \times N_{RPI}$ detected intensities are correctly dealt with through the likelihood function, which does not suffer from truncation issues. In order to get the most accurate recorded intensities, it is best to avoid working with dose levels that lead to this plateau. If we need to use GS for computational efficiency, we can do so by choosing $N_{\text{RPI}} = 2$ for low-dose cases. Another option is to use ML and a higher value of N_{RPI} to make full use of the available information. However, this will require longer computation time and does not lead to a significant error reduction. Note that the plateau is also misleading here, as it could lead to the assumption that the lower plateau level for higher N_{RPI} is a desirable suppression of the noise. However, it is merely a truncation or phase-wrapping artifact that obfuscates the actual signal.

When we examine the visual output of the retrieved phase for the cameraman object in Figure 5, we can clearly see some significant differences between ZPC and RPI. At the highest dose, both methods accurately retrieve all object details. In the case of ZPC, the intensity is dispersed outside the illuminated region of interest, which makes it less effective than the diffraction-based method. We discovered that only 62.5% of the intensity is within the region of interest, with the remaining 37.5% not contributing useful information from the object. At low doses (marked with a \star in Fig. 5), the ZPC displays a flat phase of -10/8 rad wherever no electron was detected. While this flat value may seem like low noise due to the absence of contrast variation, in reality, it indicates a lack of information in those areas. This is why we observe a plateau in Figure 4 for ZPC. In the case of GS RPI, this effect also arises from phase wrapping of the noise, but it is less prominent, which is also visible in the figure indicated with a * in Figure 5 for RPI.

Furthermore, we also show the detected intensity for the ZPC case to demonstrate the normalization effect that was derived in this paper. Figure 6 shows the detected intensity of the random phase object of 64 × 64. As mentioned before, with correct oversampling of C = 1/2, we notice the intensity outside of the illuminated area to be 37.5% of the total illumination intensity. This effect occurs as a result of the phase discontinuity that is essential for ZPC to work but leads to a decrease in dose efficiency as only a fraction of all electrons take part in the actual formation of the central phase encoded part of the image and, even there, the contrast is lower. Omitting this oversampling by 2 in all directions will wrongly create an aliasing of the reference part of the wave, which will result in a seemingly 50/50 distribution between the object and the reference part of the wave. This distribution will result in much better counting statistics, but it is an aliasing artifact that cannot be reproduced in an actual experiment.

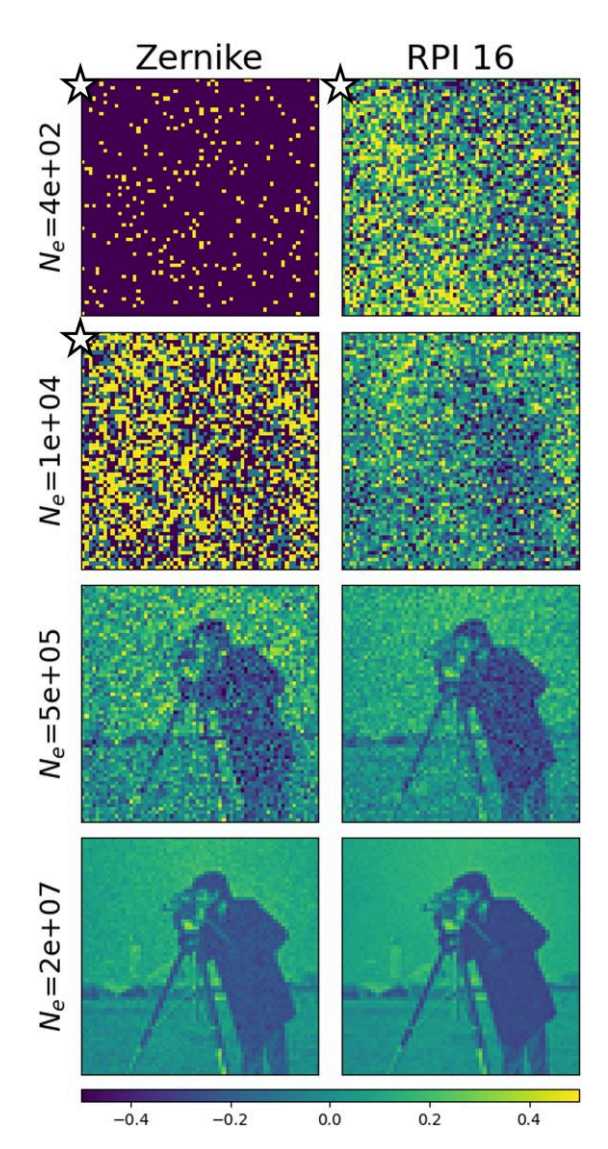


Fig. 5. Comparison of ZPC and GS RPI phase retrieval as a function of dose on a more realistic 2D object. At high doses, both methods retrieve the object effectively. The top figures marked with a \star do not adhere to the color bar scaling to aid visualization.

Discussion

Following the previous derivation and results, we can now extract common features from these numerical exercises and discuss the effect of each parameter on the reconstruction.

The Role of Dose

The role of dose clearly follows the expected $1/\sqrt{N_e/N}$ trend, albeit with different pre-factors for either ZPC or diffraction-based measurements. This trend shows that more electrons are obviously better and that the number of detector pixels M should be carefully balanced against the required sampling and desired field of view. We observe a deviating trend at a very low dose due to phase wrapping, which truncates the phase error and leads to a plateau in the error prediction. This plateau indicates a situation where noise is maximized, and it is unlikely that one would recover any meaningful signal in this range. We observed that this truncation effect is more severe for the GS RPI method as it acts on the $N_{\rm RPI}$ individual

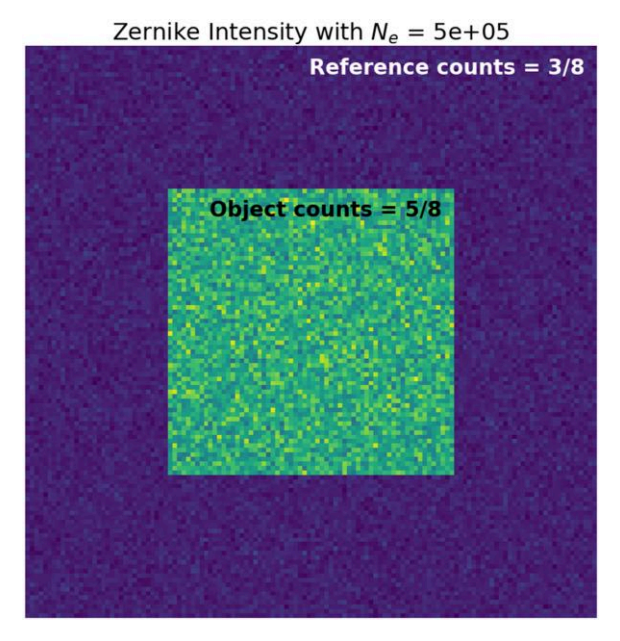


Fig. 6. Example of a correctly sampled ZPC image of a random phase object of 64×64 zero-padded to 128×128 with $N_e = 5 \times 10^5$. The central 64×64 area contains the actual phase-related image and 5/8 of the total dose with which the object was illuminated. The other 3/8 lands outside the central area and does not contribute to the desired information.

experiments, while this does not appear for the ML RPI method. This finding is significant, as it guides the experimenter to use a lower $N_{\rm RPI}$ for very low-dose imaging to optimally distribute the available dose among each phase configuration in the illumination. Ideally, ML RPI would always be used, but our current implementation is too slow to be practical on realistically sized objects. Further algorithm development in this direction would be useful. As a side note, we speculate that these effects also occur for ptychography with overlapping probes, as also here, one records multiple instances of the same part of the object with different phase encoding (Li et al., 2014; O'Leary et al., 2020, 2021; Leidl et al., 2024).

Is RPI the Best we can do?

In our study, we employed the RPI method to solve the issue of under-determination in the inverse problem, which helps eliminate translation and point symmetry uncertainties (Fannjiang & Liao, 2012). Although this method provides a fivefold improvement over ZPC, it raises the question of whether it would be more efficient to devise a new illumination scheme based on insights gained from previous experiments rather than recording 16 random phase illumination variants. We explored variations of this approach, such as using the complex conjugate of the current phase estimate, employing orthogonal basis sets like Hadamard and Fourier, and using only $\pm \pi$ phase illumination akin to a charge flipping algorithm (Fienup, 1982). However, these attempts yielded nearly identical results to our simpler random phase illumination scheme.

It is intriguing to consider how we can efficiently encode a phase message using N_e electrons. Assuming that each electron represents one bit of information, then N_e electrons could

convey a message with 2^{N_e} variations. If we distribute this across the $N = (n \times n)$ independent pixels, we get:

$$\sigma_{\phi, \text{binary}} = \frac{2\pi}{2\frac{N_e}{\nu^2}}.$$
 (14)

This encoding would be significantly more efficient in terms of electron dose, but assumes that:

- We know exactly when an electron is interacting with the sample in order to encode a zero bit when no detecting occurs.
- We have a way to control the phase of the incoming electron wave precisely.
- We have a way to set up an experiment to find out if the modulo of the phase shift of the sample with respect to the local incoming phase of the wave is higher or lower than some value.

This scheme could be approached when multiple passes of the same electron through the sample can be configured as proposed in the quantum microscope (Kruit et al., 2016; Juffmann et al., 2017; Koppell et al., 2019; Turner et al., 2021) and even further improvement is expected when using *squeezed* or entangled electron states (Koppell et al., 2022). The practical implementation of this seems currently highly challenging. Still, it is good to keep in mind that the results in this paper may differ from what is possible.

Technological Difficulties to Realize This

In this paper, we have looked at the fundamental counting noise limits and have assumed that we can create an ideal phase plate acting on the phase of the illuminating wave and an ideal but correctly normalized version of the ZPC that acts on the exit wave in the back focal plane. Several technological obstacles have to be overcome in order to realize these ultimate predictions for the ZPC case:

- The ideal Airy disc-like Zernike phase profile is difficult to realize.
- The ideal Zernike phase shift may differ from $\pi/2$ (see Beleggia, 2008).
- The ZPP profile should adapt in width to the illumination size to obtain the best performance while avoiding loss of low frequencies.

Also, for the RPI, several obstacles will hinder a straightforward implementation:

• A programmable phase plate has considerable limitations regarding the fill factor (Verbeeck et al., 2018; Vega Ibáñez et al., 2023; Yu et al., 2023), meaning that we also imprint amplitude modulation into the probe. However, this may or may not be beneficial in some cases (Allars et al., 2021; You et al., 2023). This could be overcome by scanning the amplitude and phase-modulated probe in ptychography style to illuminate all the areas of the sample with some overlap between the probe positions.

In both scenarios, charging problems, gradual drift, and contamination are potential issues.

A Note on Re-Normalization

In our paper, we have examined a sample as a collection of random phases without making any assumptions about the relationship between pixels or the probability of certain patterns occurring. In reality, the set of actual images is smaller than the total number of potential random phase formations. In other words, there is some underlying regularity in the sample. If we correctly describe this regularity, we can significantly gain in terms of signal-to-noise as this constitutes prior knowledge about the sample (Maiden et al., 2017, 2024; Schloz et al., 2020; Diederichs et al., 2024; Leidl et al., 2024). However, we need to be careful and compare similar situations. For example, if we use regularization in an RPI setup, we should use the same assumptions in the case of ZPC. Failing to do so will inevitably lead to biased opinions, as was the case in compressed sensing (Donoho, 2006; Leary et al., 2013; Li et al., 2018), which also relies on regularization arguments. This makes it impossible to compare to a situation where normal sampling is applied unless the regularization prior is included (Van den Broek et al., 2019). For this reason, we will not discuss regularization here. However, significant gains can be achieved if such prior knowledge is available and valid (Diederichs et al., 2024).

Conclusion

We have demonstrated that there is a clear benefit in terms of counting statistics in recording multiple diffraction patterns over the more conventional ZPC imaging. We stress here that we have shown just one possible way of improving the dose efficiency of ZPC imaging without making claims on related ptychographic or other diffraction-based setups. Nevertheless, breaking this limit for one case demonstrates that ZPC is not the ultimate limit, and this should invite further research. Note also that we have assumed the weak phase object approximation throughout, which is known to be a very limiting assumption in practice. We found the benefit in terms of dose efficiency to be a factor of 5, which would allow a very significant shifting of the beam damage boundaries that are hindering progress in, e.g., life sciences, but also in many materials science areas such as battery materials, polymer science, zeolites, perovskites, metal-organic frameworks and many more.

This improvement factor is mainly attributed to a subtle normalization issue that occurs in ZPC imaging. This issue makes ZPC less dose efficient, as it seems to be the case if we make a fair comparison where the sample is illuminated with exactly the same dose over exactly the same area of illumination. This paper avoids discussing actual implementation details, and it might well be possible to improve this benefit further if, e.g., the illumination can be updated to take into account information from the partial experiment that was already performed. Whether the gain from the diffractionbased recordings proposed here can also be obtained in practice remains to be seen, as many practical details will influence the actual dose efficiency. Nevertheless, there has been much promising progress in ptychography over the last few years, and it relies on diffraction-based detection, albeit with a different illumination scheme than the RPI suggested here.

One potential advantage of detecting in the diffraction plane while adjusting the phase of the probe is the potential for a simpler, smaller, and more cost-effective electron microscope specifically designed for life science imaging. In this scenario, the camera could have significantly fewer pixels, and the projector system could be completely removed (along with the image corrector), as long as some form of scanning system or phase plate can quickly alter the illumination. This discovery shows promise for affordable tabletop instruments that could expand the information we can gather from beamsensitive nanoscale objects.

Availability of Data and Materials

The authors have declared that no datasets apply for this piece.

Author Contributions Statement

F.V.I. performed coding of the GS algorithm, numerical exercises, creation of figures, and general writing. J.V. performed derivations in appendices, general conceptualization, coding of ML 1D and 2D simulations, creation of figures, and general writing.

Financial Support

J.V. and F.V.I acknowledge funding from the Flemish Science Fund, FWO G042820N 'Exploring adaptive optics in transmission electron microscopy.' J.V. acknowledges funding through the IMPRESS project, which received funding from the HORIZON EUROPE framework program for research and innovation under grant agreement no. 101094299.

Conflict of Interest

J.V. declares to have a financial interest in AdaptEM BV (AdaptEM, 2021), a spinoff company from the University of Antwerp that produces adaptive phase plates for the EM market.

References

Abregana TJ & Almoro PF (2022). Phase retrieval by amplitude modulation using digital micromirror device. *Opt Lasers Eng* 150, 106851. https://doi.org/10.1016/j.optlaseng.2021.106851

AdaptEM (2021). https://adaptem.eu.

Allars F, Lu PH, Kruth M, Dunin-Borkowski RE, Rodenburg JM & Maiden AM (2021). Efficient large field of view electron phase imaging using near-field electron ptychography with a diffuser. Ultramicroscopy 231, 113257. https://doi.org/10.1016/j.ultramic. 2021.113257

Allen LJ, Alfonso AJD & Findlay SD (2015). Modelling the inelastic scattering of fast electrons. *Ultramicroscopy* **151**, 11–22. https://doi.org/10.1016/j.ultramic.2014.10.011

Aster RC, Borchers B & Thurber CH (2018). Parameter Estimation and Inverse Problems, (3rd ed.). Amsterdam: Elsevier.

Barlow RJ (1991). A Guide to the Use of Statistical Methods in the Physical Sciences. Chichester: John Wiley & Sons.

Beleggia M (2008). A formula for the image intensity of phase objects in Zernike mode. *Ultramicroscopy* **108**(9), 953–958. https://doi.org/10.1016/j.ultramic.2008.03.003

Bettens E, Van Dyck D & Sijbers J (1999). Model-based two-object resolution from observations having counting statistics. *Ultramicroscopy* 77(1-2), 37–48. https://doi.org/10.1016/S0304-3991(99)00006-6

Beyer A, Krause FF, Robert HL, Firoozabadi S, Grieb T, Kükelhan P, Heimes D, Schowalter M, Müller-Caspary K, Rosenauer A & Volz K (2020). Influence of plasmon excitations on atomic-resolution

- quantitative 4D scanning transmission electron microscopy. *Sci Rep* **10**(1), 17890. https://doi.org/10.1038/s41598-020-74434-w
- Bouchet D, Dong J, Maestre D & Juffmann T (2021). Fundamental bounds on the precision of classical phase microscopes. *Phys Rev Appl* 15(2), 024047. https://doi.org/10.1103/PhysRevApplied.15. 024047
- Brown HG, Chen Z, Weyland M, Ophus C, Ciston J, Allen LJ & Findlay SD (2018). Structure retrieval at atomic resolution in the presence of multiple scattering of the electron probe. *Phys Rev Lett* **121**(26), 266102. https://doi.org/10.1103/PhysRevLett.121.266102
- Chari A & Stark H (2023). Prospects and limitations of high-resolution single-particle cryo-electron microscopy. *Annu Rev Biophys* **52**(1), 391–411. https://doi.org/10.1146/biophys.2023.52.issue-1
- Chen M, Ren D, Liu HY, Chowdhury S & Waller L (2020). Multi-layer born multiple-scattering model for 3D phase microscopy. *Optica* 7(5), 394–403. https://doi.org/10.1364/OPTICA.383030
- Chen JZ, Sachse C, Xu C, Mielke T, Spahn CM & Grigorieff N (2008). A dose-rate effect in single-particle electron microscopy. *J Struct Biol* **161**(1), 92–100. https://doi.org/10.1016/j.jsb.2007.09.017
- Chen Z, Shao YT, Zeltmann SE, Harikrishnan KP, Rosenberg ER, Ross CA, Jiang Y & Muller DA (2024). 'Imaging interstitial atoms with multislice electron ptychography.' arXiv, arXiv:2407.18063, preprint: not peer reviewed.
- Coene W, Janssen G, de Beeck MO & Van Dyck D (1992). Phase retrieval through focus variation for ultra-resolution in field-emission transmission electron microscopy. *Phys Rev Lett* 69(26), 3743–3746. https://doi.org/10.1103/PhysRevLett.69.3743
- Cramer H (1946). Mathematical Methods of Statistics. Princeton: Princeton University Press.
- Danev R, Buijsse B, Khoshouei M, Plitzko JM & Baumeister W (2014). Volta potential phase plate for in-focus phase contrast transmission electron microscopy. *Proc Natl Acad Sci U S A* 111(44), 15635–15640. https://doi.org/10.1073/pnas.1418377111
- Danev R & Nagayama K (2001). Transmission electron microscopy with Zernike phase plate. *Ultramicroscopy* 88(4), 243–252. https://doi.org/10.1016/S0304-3991(01)00088-2
- Danev R & Nagayama K (2008). Single particle analysis based on Zernike phase contrast transmission electron microscopy. J Struct Biol 161, 211–218. https://doi.org/10.1016/j.jsb.2007.10.015
- Danev R, Tegunov D & Baumeister W (2017). Using the Volta phase plate with defocus for cryo-EM single particle analysis. *Elife* 6, e23006. https://doi.org/10.7554/eLife.23006
- De Backer A, Van Aert S & Van Dyck D (2011). High precision measurements of atom column positions using model-based exit wave reconstruction. *Ultramicroscopy* **111**, 1475–1482. https://doi.org/10.1016/j.ultramic.2011.07.002
- Den Dekker A, Van Aert S, Van den Bos A & Van Dyck D (2005). Maximum likelihood estimation of structure parameters from high resolution electron microscopy images. part I: A theoretical framework. *Ultramicroscopy* 104, 83–106. https://doi.org/10.1016/j. ultramic.2005.03.001
- den Dekker A, Van Aert S, Van Dyck D & Geuens P (2001). Does a monochromator improve the precision in quantitative HRTEM? *Ultramicroscopy* 89, 275–290. https://doi.org/10.1016/S0304-3991(01)00089-4
- Diederichs B, Herdegen Z, Strauch A, Filbir F & Müller-Caspary K (2024). Exact inversion of partially coherent dynamical electron scattering for picometric structure retrieval. *Nat Commun* 15, 101. https://doi.org/10.1038/s41467-023-44268-x
- Donoho DL (2006). Compressed sensing. IEEE Trans Inf Theory 52, 1289–1306. https://doi.org/10.1109/TIT.2006.871582
- Drenth A, Huiser A & Ferwerda H (1975). The problem of phase retrieval in light and electron microscopy of strong objects. *Opt Acta (Lond)* 22(7), 615–628. https://doi.org/10.1080/713819083
- Dwyer C (2005). Multislice theory of fast electron scattering incorporating atomic inner-shell ionization. *Ultramicroscopy* **104**(2), 141–151. https://doi.org/10.1016/j.ultramic.2005.03.005

- Dwyer C (2023). Quantum limits of transmission electron microscopy. *Phys Rev Lett* **130**(5), 056101. https://doi.org/10.1103/PhysRevLett. 130.056101
- Dwyer C, Findlay SD & Allen LJ (2008). Multiple elastic scattering of core-loss electrons in atomic resolution imaging. *Phys Rev B Condens Matter Mater Phys* 77, 184107. https://doi.org/10.1103/ PhysRevB.77.184107
- Dwyer C & Paganin DM (2024). Quantum and classical fisher information in four-dimensional scanning transmission electron microscopy. *Phys Rev B* 110, 024110. https://doi.org/10.1103/PhysRevB. 110.024110
- Egerton R (2007). Limits to the spatial, energy and momentum resolution of electron energy-loss spectroscopy. *Ultramicroscopy* **107**, 575–586. https://doi.org/10.1016/j.ultramic.2006.11.005
- Egerton RF (2012). Mechanisms of radiation damage in beam-sensitive specimens, for TEM accelerating voltages between 10 and 300 kv. *Microsc Res Tech* 75(11), 1550–1556. https://doi.org/10.1002/jemt.v75.11
- Egerton R (2013). Control of radiation damage in the TEM. *Ultramicroscopy* **127**, 100–108. https://doi.org/10.1016/j.ultramic. 2012.07.006
- Egerton R (2017). Scattering delocalization and radiation damage in STEM-EELS. *Ultramicroscopy* **180**, 1–10. https://doi.org/10.1016/j.ultramic.2017.02.007
- Elser V, Lan TY & Bendory T (2018). Benchmark problems for phase retrieval. SIAM J Imaging Sci 11(4), 2429–2455. https://doi.org/10.1137/18M1170364
- Fannjiang A & Liao W (2012). Phase retrieval with random phase illumination. J Opt Soc Am A 29, 1847. https://doi.org/10.1364/ JOSAA.29.001847
- Faulkner HML & Rodenburg JM (2004). Movable aperture lensless transmission microscopy: A novel phase retrieval algorithm. *Phys Rev Lett* **93**, 023903. https://doi.org/10.1103/PhysRevLett.93. 023903
- Fienup JR (1982). Phase retrieval algorithms: A comparison. *Appl Opt* 21, 2758. https://doi.org/10.1364/AO.21.002758
- Fienup JR (1993). Phase-retrieval algorithms for a complicated optical system. *Appl Opt* **32**, 1737–1746. https://doi.org/10.1364/AO.32.001737
- Gerchberg RW (1972). A practical algorithm for the determination of phase from image and diffraction plane pictures. *Optik (Stuttg)* 35, 237–246. https://api.semanticscholar.org/CorpusID:55691159.
- Glaeser RM (1971). Limitations to significant information in biological electron microscopy as a result of radiation damage. *J Ultrastruct Res* 36, 466–482. https://doi.org/10.1016/S0022-5320(71)80118-1
- Gonsalves RA (1982). Phase retrieval and diversity in adaptive optics. *Opt Eng* **21**, 829–832. https://doi.org/10.1117/12.7972989
- Guizar-Sicairos M & Fienup JR (2012). Understanding the twin-image problem in phase retrieval. *J Opt Soc Am A* **29**(11), 2367–2375. https://doi.org/10.1364/JOSAA.29.002367
- Gureyev TE, Nesterets YI, Paganin D, Pogany A & Wilkins S (2006). Linear algorithms for phase retrieval in the fresnel region. 2. partially coherent illumination. *Opt Commun* 259, 569–580. https://doi.org/10.1016/j.optcom.2005.09.072
- Hadamard J (1893). Resolution d'une question relative aux determinants. *Bull Sci Math* 2, 240–246. https://www.scirp.org/reference/referencespapers?referenceid=1839681
- Huang G, Wu D, Luo J, Lu L, Li F, Shen Y & Li Z (2020). Generalizing the Gerchberg–Saxton algorithm for retrieving complex optical transmission matrices. *Photonics Res* 9, 34–42. https://doi.org/10. 1364/PRJ.406010
- Jannis D, Velazco A, Béché A & Verbeeck J (2022). Reducing electron beam damage through alternative STEM scanning strategies, part II: Attempt towards an empirical model describing the damage process. *Ultramicroscopy* 240, 113568. https://doi.org/10.1016/j.ultramic. 2022.113568
- Juffmann T, Koppell SA, Klopfer BB, Ophus C, Glaeser RM & Kasevich MA (2017). Multi-pass transmission electron microscopy. Sci Rep 7, 1699. https://doi.org/10.1038/s41598-017-01841-x

- Koppell SA, Israel Y, Bowman AJ, Klopfer BB & Kasevich MA (2022). Transmission electron microscopy at the quantum limit. *Appl Phys Lett* **120**, 190502. https://doi.org/10.1063/5.0086148
- Koppell S & Kasevich M (2021). Information transfer as a framework for optimized phase imaging. Optica 8, 493–501. https://doi.org/ 10.1364/OPTICA.412129
- Koppell SA, Mankos M, Bowman AJ, Israel Y, Juffmann T, Klopfer BB & Kasevich MA (2019). Design for a 10 kev multi-pass transmission electron microscope. *Ultramicroscopy* 207, 112834. https://doi.org/10.1016/j.ultramic.2019.112834
- Kruit P, Hobbs R, Kim CS, Yang Y, Manfrinato V, Hammer J, Thomas S, Weber P, Klopfer B, Kohstall C, Juffmann T, Kasevich M, Hommelhoff P & Berggren K (2016). Designs for a quantum electron microscope. *Ultramicroscopy* 164, 31–45. https://doi.org/10.1016/j.ultramic.2016.03.004
- Küçükoğlu B, Mohammed I, Guerrero-Ferreira RC, Kube M, Radecke J, Ribet SM, Varnavides G, Leidl ML, Lau K, Nazarov S, Myasnikov A, Sachse C, Müller-Caspary K, Ophus C & Stahlberg H (2024). Low-dose cryo-electron ptychography of proteins at sub-nanometer resolution. *Nat Commun* 15, 8062. https://doi.org/10.1038/s41467-024-52403-5.
- Leary R, Saghi Z, Midgley PA & Holland DJ (2013). Compressed sensing electron tomography. *Ultramicroscopy* 131, 70–91. https://doi.org/10.1016/j.ultramic.2013.03.019
- Leidl ML, Diederichs B, Sachse C & Müller-Caspary K (2024). Influence of loss function and electron dose on ptychography of 2D materials using the wirtinger flow. *Micron* 185, 103688. https://doi.org/10.1016/j.micron.2024.103688
- Leidl ML, Sachse C & Müller-Caspary K (2023). Dynamical scattering in ice-embedded proteins in conventional and scanning transmission electron microscopy. *IUCrJ* 10, 475–486. https://doi.org/10.1107/ S2052252523004505
- Li X, Dyck O, Kalinin SV & Jesse S (2018). Compressed sensing of scanning transmission electron microscopy (STEM) with nonrectangular scans. *Microsc Microanal* 24(6), 623–633. https://doi.org/10.1017/S143192761801543X
- Li P, Edo TB & Rodenburg JM (2014). Ptychographic inversion via Wigner distribution deconvolution: Noise suppression and probe design. *Ultramicroscopy* 147, 106–113. https://doi.org/10.1016/j. ultramic.2014.07.004
- Lichte H & Lehmann M (2007). Electron holography-basics and applications. Rep Prog Phys 71, 016102. https://doi.org/10.1088/0034-4885/71/1/016102
- Liu C, Walther T & Rodenburg J (2009). Influence of thick crystal effects on ptychographic image reconstruction with moveable illumination. *Ultramicroscopy* 109, 1263–1275. https://doi.org/10.1016/j.ultramic.2009.05.017
- Maiden AM, Humphry MJ & Rodenburg JM (2012). Ptychographic transmission microscopy in three dimensions using a multi-slice approach. J Opt Soc Am A Opt Image Sci Vis 29, 1606–1614. https:// doi.org/10.1364/JOSAA.29.001606
- Maiden A, Johnson D & Li P (2017). Further improvements to the ptychographical iterative engine. Optica 4, 736. https://doi.org/10. 1364/OPTICA.4.000736
- Maiden AM, Mei W & Li P (2024). WASP: Weighted average of sequential projections for ptychographic phase retrieval. Opt Express 32, 21327. https://doi.org/10.1364/OE.516946
- Maiden AM & Rodenburg JM (2009). An improved ptychographical phase retrieval algorithm for diffractive imaging. *Ultramicroscopy* 109, 1256–1262. https://doi.org/10.1016/j.ultramic.2009.05.012
- Malac M, Hettler S, Hayashida M, Kano E, Egerton RF & Beleggia M (2021). Phase plates in the transmission electron microscope: Operating principles and applications. *Microscopy* 70, 75–115. https://doi.org/10.1093/jmicro/dfaa070
- Mao W, Zhang W, Huang C, Zhou L, Kim JS, Gao S, Lei Y, Wu X, Hu Y, Pei X, Fang W, Liu X, Song J, Fan C, Nie Y, Kirkland AI & Wang P (2024). 'Multi-convergence-angle ptychography with simultaneous strong contrast and high resolution.' arXiv, arXiv:2403.16902, preprint: not peer reviewed.

- Martin A, Chen FR, Hsieh WK, Kai JJ, Findlay S & Allen L (2006). Spatial incoherence in phase retrieval based on focus variation. Ultramicroscopy 106, 914–924. https://doi.org/10.1016/j.ultramic. 2006.04.008
- McCallum B & Rodenburg J (1992). Two-dimensional demonstration of Wigner phase-retrieval microscopy in the STEM configuration. *Ultramicroscopy* 45, 371–380. https://doi.org/10.1016/0304-3991(92)90149-E
- McCallum B & Rodenburg J (1993). Simultaneous reconstruction of object and aperture functions from multiple far-field intensity measurements. *J Opt Soc Am A Opt Image Sci Vis* **10**, 231–239. https://doi.org/10.1364/JOSAA.10.000231
- Melnyk O (2023). 'Convergence properties of gradient methods for blind ptychography.' arXiv, arXiv:2306.08750, preprint: not peer reviewed.
- Müller-Caspary K, Krause FF, Winkler F, Béché A, Verbeeck J, Van Aert S & Rosenauer A (2019). Comparison of first moment STEM with conventional differential phase contrast and the dependence on electron dose. *Ultramicroscopy* 203, 95–104. https://doi.org/10.1016/j.ultramic.2018.12.018
- Muller D & Silcox J (1995). Delocalization in inelastic scattering. *Ultramicroscopy* **59**, 195–213. https://doi.org/10.1016/0304-3991(95)00029-Z
- Nakane T, Kotecha A, Sente A, McMullan G, Masiulis S, Brown PM, Grigoras IT, Malinauskaite L, Malinauskas T, Miehling J, Uchanski T, Yu L, Karia D, Pechnikova EV, de Jong E, Keizer J, Bischoff M, McCormack J, Tiemeijer P, Hardwick SW, Chirgadze DY, Murshudov G, Aricescu AR & Scheres SHW (2020). Single-particle cryo-EM at atomic resolution. *Nature* 587, 152–156. https://doi.org/10.1038/s41586-020-2829-0
- Nellist PD, McCallum BC & Rodenburg JM (1995). Resolution beyond the 'information limit' in transmission electron microscopy. *Nature* 374, 630–632. https://doi.org/10.1038/374630a0
- Nellist P & Rodenburg J (1994). Beyond the conventional information limit: The relevant coherence function. *Ultramicroscopy* **54**, 61–74. https://doi.org/10.1016/0304-3991(94)90092-2
- O'Leary C, Allen C, Huang C, Kim J, Liberti E, Nellist P & Kirkland A (2020). Phase reconstruction using fast binary 4D STEM data. *Appl Phys Lett* 116, 124101. https://doi.org/10.1063/1.5143213.
- O'Leary CM, Martinez GT, Liberti E, Humphry MJ, Kirkland AI & Nellist PD (2021). Contrast transfer and noise considerations in focused-probe electron ptychography. *Ultramicroscopy* **221**, 113189. https://doi.org/10.1016/j.ultramic.2020.113189
- Oxley MP & Dyck OE (2020). The importance of temporal and spatial incoherence in quantitative interpretation of 4D-STEM. *Ultramicroscopy* 215, 113015. https://doi.org/10.1016/j.ultramic. 2020.113015
- Parvizi A, Müller J, Funken S & Koch C (2015). A practical way to resolve ambiguities in wavefront reconstructions by the transport of intensity equation. *Ultramicroscopy* 154, 1–6. https://doi.org/10.1016/j.ultramic.2015.02.015
- Pei X, Zhou L, Huang C, Boyce M, Kim JS, Liberti E, Hu Y, Sasaki T, Nellist PD, Zhang P, Stuart DI, Kirkland AI & Wang P (2023). Cryogenic electron ptychographic single particle analysis with wide bandwidth information transfer. *Nat Commun* 14, 3027. https://doi.org/10.1038/s41467-023-38268-0
- Pelz PM, Qiu WX, Bücker R, Kassier G & Miller RJD (2017). Low-dose cryo electron ptychography via non-convex Bayesian optimization. Sci Rep 7, 9883. https://doi.org/10.1038/s41598-017-07488-y
- Rao CR (1945). Information and the accuracy attainable in the estimation of statistical parameters. *Bull Calcutta Math Soc* 37, 81–89.
- Ren D, Ophus C, Chen M & Waller L (2020). A multiple scattering algorithm for three dimensional phase contrast atomic electron tomography. *Ultramicroscopy* 208, 112860. https://doi.org/10.1016/j.ultramic.2019.112860
- Robert H, Lobato I, Lyu F, Chen Q, Van Aert S, Van Dyck D & Müller-Caspary K (2022). Dynamical diffraction of high-energy electrons investigated by focal series momentum-resolved scanning

transmission electron microscopy at atomic resolution. *Ultramicroscopy* **233**, 113425. https://doi.org/10.1016/j.ultramic. 2021.113425

Rodenburg J, McCallum B & Nellist P (1993). Experimental tests on double-resolution coherent imaging via stem. *Ultramicroscopy* 48, 304–314. https://doi.org/10.1016/0304-3991(93)90105-7

Schloz M, Pekin TC, Chen Z, Van den Broek W, Muller DA & Koch CT (2020). Overcoming information reduced data and experimentally uncertain parameters in ptychography with regularized optimization. Opt Express 28, 28306. https://doi.org/10.1364/OE.396925

Thibault P & Menzel A (2013). Reconstructing state mixtures from diffraction measurements. *Nature* 494, 68–71. https://doi.org/10.1038/ nature11806

Tolimieri R, An M & Lu C (2012). *Mathematics of Multidimensional Fourier Transform Algorithms*. New York, USA: Springer Science & Business Media.

Turner AE, Johnson CW, Kruit P & McMorran BJ (2021). Interaction-free measurement with electrons. *Phys Rev Lett* 127(11), 110401. https://doi.org/10.1103/PhysRevLett.127.110401 Unknown (1978). https://hdl.handle.net/1721.3/195767.

Van den Bos A (1989). Estimation of fourier coefficients. *IEEE Trans Instrum Meas* 38(5), 1005–1007. https://doi.org/10.1109/19.39045

Van den Broek W, Reed BW, Beche A, Velazco A, Verbeeck J & Koch CT (2019). Various compressed sensing setups evaluated against Shannon sampling under constraint of constant illumination. IEEE Trans Comput Imaging 5, 502–514. https://doi.org/10.1109/TCI.6745852

Vega Ibáñez F, Béché A & Verbeeck J (2023). Can a programmable phase plate serve as an aberration corrector in the transmission electron microscope (TEM)? *Microsc Microanal* 29, 341–351. https:// doi.org/10.1017/S1431927622012260

Velazco A, Béché A, Jannis D & Verbeeck J (2022). Reducing electron beam damage through alternative STEM scanning strategies, part i: Experimental findings. *Ultramicroscopy* 232, 113398. https://doi. org/10.1016/j.ultramic.2021.113398

Verbeeck J (2024). https://github.com/joverbee/pyEELSMODEL.

Verbeeck J, Béché A, Müller-Caspary K, Guzzinati G, Luong MA & Den Hertog M (2018). Demonstration of a 2×2 programmable phase plate for electrons. *Ultramicroscopy* **190**, 58–65. https://doi.org/10.1016/j.ultramic.2018.03.017

Verbeeck J & Van Aert S (2004). Model based quantification of EELS spectra. *Ultramicroscopy* 101, 207–224. https://doi.org/10.1016/j.ultramic.2004.06.004

Verbeeck J & Vega F (2024). Python phase retrieval module.

Yang G, Dong B, Gu B, Zhuang J & Ersoy OK (1994). Gerchberg–Saxton and Yang–Gu algorithms for phase retrieval in a nonunitary transform system: A comparison. *Appl Opt* 33, 209–218. https://doi.org/10.1364/AO.33.000209

Yang H, Pennycook TJ & Nellist PD (2015). Efficient phase contrast imaging in STEM using a pixelated detector. Part II: Optimisation of imaging conditions. *Ultramicroscopy* **151**, 232–239. https://doi.org/10.1016/j.ultramic.2014.10.013

Yoshioka H (1957). Effect of inelastic waves on electron diffraction. J Phys Soc Jap 12, 618–628. https://doi.org/10.1143/JPSJ.12.618

You S, Lu PH, Schachinger T, Kovács A, Dunin-Borkowski RE & Maiden AM (2023). Lorentz near-field electron ptychography. Appl Phys Lett 123, 192406. https://doi.org/10.1063/5.0169788

Yu CP, Vega Ibañez F, Béché A & Verbeeck J (2023). Quantum wavefront shaping with a 48-element programmable phase plate for electrons. SciPost Phys 15, 223. https://doi.org/10.21468/SciPostPhys

Zalevsky Z, Mendlovic D & Dorsch RG (1996). Gerchberg–Saxton algorithm applied in the fractional fourier or the fresnel domain. *Opt Lett* 21, 842–844. https://doi.org/10.1364/OL.21.000842

Zernike F (1942a). Phase contrast, a new method for the microscopic observation of transparent objects. *Physica* **9**, 686–698. https://doi.org/10.1016/S0031-8914(42)80035-X

Zernike F (1942b). Phase contrast, a new method for the microscopic observation of transparent objects part II. *Physica* **9**, 974–986. https://doi.org/10.1016/S0031-8914(42)80079-8

Zhou L, Song J, Kim JS, Pei X, Huang C, Boyce M, Mendonça L, ClareD, Siebert A, Allen CS, Liberti E, Stuart D, Pan X, Nellist PD, Zhang P, Kirkland AI & Wang P (2020). Low-dose phase retrieval of biological specimens using cryo-electron ptychography. Nat Commun 11(1), 2773. https://doi.org/10.1038/s41467-020-16391-6

APPENDIX A Zernike Contrast with Proper Normalization

Assume a circular area of illumination on a sample with radius R.

$$M(r) = \Pi\left(\frac{r}{2R}\right). \tag{A.1}$$

With $\Pi(x)$ the Heavyside Pi step function (or rect function) being one for $|x| < \frac{1}{2}$. The sample transmission function can be approximated as a phase object:

$$O(\mathbf{r}) = e^{i\phi(\mathbf{r})}. (A.2)$$

In the back focal plane of the sample, this will result in

$$\Psi(\mathbf{k}) = \tilde{M}(\mathbf{k}) \otimes \tilde{O}(\mathbf{k}) = \frac{2J_1(kR)}{kR} \otimes \tilde{O}(\mathbf{k}).$$
 (A.3)

With $\tilde{\ }$ designating the Fourier transformed function and J_1 a Bessel function of the first kind. Typically, experimental realizations of a ZPP in the TEM, such as the Volta Phase Plate, have an Airy-like smooth phase profile (Danev et al., 2014, 2017; Malac et al., 2021). However, to create an idealized ZPP, we assume a maximum passband frequency $k_{\rm max}$, representing the ultimate spatial resolution, and a minimum frequency k_Z , below which we introduce the required phase shift of $\pi/2$, modeled as a Heavyside Pi step function as well. A genuinely ideal ZPP will have $k_Z \longrightarrow 0$ and $k_{\rm max} \longrightarrow \infty$. However, we will see later that these parameters play an important role in normalization and are critical for discussing quantum information.

$$Z(\mathbf{k}) = \Pi\left(\frac{k}{2k_{\text{max}}}\right) \exp\left[i\frac{\pi}{2}\Pi\left(\frac{k}{2k_z}\right)\right]. \tag{A.4}$$

For $k_{\text{max}} > k_z$ and we can rewrite this as:

$$Z(\mathbf{k}) = \Pi\left(\frac{k}{2k_{\text{max}}}\right) + \Pi\left(\frac{k}{2k_z}\right)(\mathbf{i} - 1). \tag{A.5}$$

Applying this phase plate in the back focal plane leads to:

$$\Psi_{Z}(\mathbf{k}) = \left[\frac{2J_{1}(kR)}{kR} \otimes \tilde{O}(\mathbf{k})\right] Z(\mathbf{k}). \tag{A.6}$$

Transforming this back to the image plane, we get:

$$\tilde{\Psi}_{Z}(\mathbf{r}) = [M(\mathbf{r})O(\mathbf{r})] \otimes \tilde{Z}(\mathbf{r}). \tag{A.7}$$

We can rewrite the Fourier transform of the ZPP as:

$$\tilde{Z}(\mathbf{r}) = \frac{2J_1(rk_{\text{max}})}{rk_{\text{max}}} + \frac{2J_1(rk_z)}{rk_z}(i-1).$$
 (A.8)

The first term will lead to a replica of the object with a spatial resolution limit of $1/k_{\rm max}$. The second term, however, will create a blurred version of the illuminated patch M by a Bessel function of width $R_Z = 1/k_Z$. This will serve as a reference wave, revealing the phase contrast when interfering with the first term. The blurring will take intensity from within the illuminated area outside the illuminated area, which carries no useful information.

This is critical for consideration of the role of counting noise, as not all electrons will contribute to the desired ZPC signal. The blurring reduces the local intensity by a factor C, which can be estimated in the center of the image as:

$$C = \int_0^{Rk_z} \frac{2J_1(k)}{k} dk$$
 (A.9)

$$= [\pi R k_z H_0(R k_z) - 2] J_1(R k_z) \tag{A.10}$$

$$+Rk_z[2-\pi H_1(Rk_z)]J_0(Rk_z)$$
 (A.11)

$$C \approx Rk_z,$$
 (A.12)

with H_0 and H_1 Struve functions of zeroth and first order, respectively. The simplification in the last step is a very good approximation when $Rk_z < 1$. If we choose $Rk_z = R/R_z \le 1/2$ (required to recover all but the DC frequency, anything higher will lead to loss of low-frequency components) we can rewrite the exit wave for $r \le R$ as

$$\Psi(\mathbf{r}, r \le R, R/R_z)$$

 $\le 1/2 = O(\mathbf{r}) + (i-1)C^2M(\mathbf{r})O(\mathbf{r}).$ (A.13)

With $C \approx R/R_z$ and $M(\mathbf{r})O(\mathbf{r})$ the averaged exit wave inside the illuminated patch M caused by the convolution of the Heavyside and Airy pattern with 'radius' R and R_z , respectively. This convolution will re-scale this reference wave by a factor C^2 because part of this wave now ends up outside the illumination patch in the image plane. Applying the weak phase approximation and assuming the phase of the object does not contain spatial frequency variations above $k_{\rm max}$:

$$O(\mathbf{r}) \approx 1 + i\phi(\mathbf{r})$$
 (A.14)

$$\Psi(\mathbf{r}, r \le R, R/R_z \le 1/2) \approx 1 + i\phi(\mathbf{r}) + (i-1)C^2$$
 (A.15)

$$\begin{split} I_z(\mathbf{r},\,r \leq R,\,R/R_z \leq 1/2) &\approx \left| \Psi(\mathbf{r},\,r \leq R,\,C \leq 1/2) \right|^2 \\ &\approx (1-C^2)^2 + (\phi(\mathbf{r}) + C^2)^2 \\ &\approx 1-2C^2 + 2C^4 + 2C^2\phi(\mathbf{r}) \\ &+ \phi(\mathbf{r})^2 \\ &\approx 1-2C^2 + 2C^4 + 2C^2\phi(\mathbf{r}) \\ &+ \dots, \end{split}$$

where we kept only linear terms in the phase. $I_z(\mathbf{r}, r \le R, C \le 1/2)$ is the observed intensity in the image plane within the illuminated area. The average intensity within the illuminated patch is $\overline{I_z(\mathbf{r}, r \le R, C \le 1/2)} \approx 1 - 2C^2 + 2C^4$. We can recover the phase from the intensity as:

$$\phi(\mathbf{r}, r \le R) \approx \frac{I_z(\mathbf{r}, r \le R) - 1 + 2C^2 - 2C^4}{2C^2}.$$
 (A.17)

In a practical implementation, the intensity will be recorded on a pixelated camera, and we assume I_z to be scaled such that if the ZPP was removed, there would be an average of 1 electron per

pixel. This allows us to estimate the standard deviation of the phase error as:

$$\sigma_{\phi} = \frac{1}{2\sqrt{N_{e}/n^{2}}} \frac{\sqrt{1 - 2C^{2} + 2C^{4}}}{C^{2}}$$
 (A.18)

Where the last term is a correction term that takes care of the role of *C*, which depends on the parameters of both illumination size and scale of the phase shifting part of the phase plate.

Appendix B Numerical Implementation of Zernike Contrast

The consequence of the above considerations for a numerical implementation of a ZPP is that zero padding around the object is essential. Omitting this step will lead to an overly optimistic result on the quantum information content that a ZPC implementation can obtain. Furthermore, this zero-padding step represents a situation where the object is periodically repeated until infinity and illuminated by an infinite plane wave. In general, we are not interested in perfectly periodic structures (otherwise, diffraction would be a far more logical choice), and even if we are, it is, in practice, impossible to make the illumination box exactly fit with periodic boundaries.

As the intensity recording involves a modulus squared, which relates to the autocorrelation in the image plane, proper zero padding is only guaranteed when there is at least padding with n/2 on all sides for an $n \times n$ illumination area. Padding more will worsen the counting statistics further; padding less will lead to an unphysical situation as it cannot be replicated in a real experiment (Fig. B.1).

We can use the crudest approximation of a ZPP in a numerical experiment by creating an $M = m \times m$ filter matrix in the discrete Fourier plane with all 1s and only the DC component in the top left corner equal to the complex i. We can decompose this filter into a sum of a matrix with all 1s and another matrix with all zeros except for the DC component, which we take as (i-1). Fourier transforming this will lead to a sum of 2 matrices, one of which has only a DC component equal to 1 and the other of which is 1, and the other being a flat matrix with elements (i-1)/M. We can now simulate the action of this filter by convolving this real space representation of the Zernike filter kernel with an object. If we choose the object first to be the same size as the filter kernel (M = N) we get:

$$\Psi_{Z}(\mathbf{r}) = O(\mathbf{r}) + M \frac{(i-1)}{M} \langle O(\mathbf{r}) \rangle \tag{B.1}$$

$$\Psi_Z(\mathbf{r}) = 1 + i\phi(\mathbf{r}) + i - 1$$
 (B.2)

$$\Psi_Z(\mathbf{r}) = \mathbf{i} + \mathbf{i}\phi(\mathbf{r}) \tag{B.3}$$

$$I_Z(\mathbf{r}) = 1 + 2\phi(\mathbf{r}) + \phi(\mathbf{r})^2 \tag{B.4}$$

$$I_Z(\mathbf{r}) \approx 1 + 2\phi(\mathbf{r}).$$
 (B.5)

From which we can derive the phase unambiguously from the intensity:

$$\phi(\mathbf{r}) \approx \frac{I_Z - 1}{2}.\tag{B.6}$$

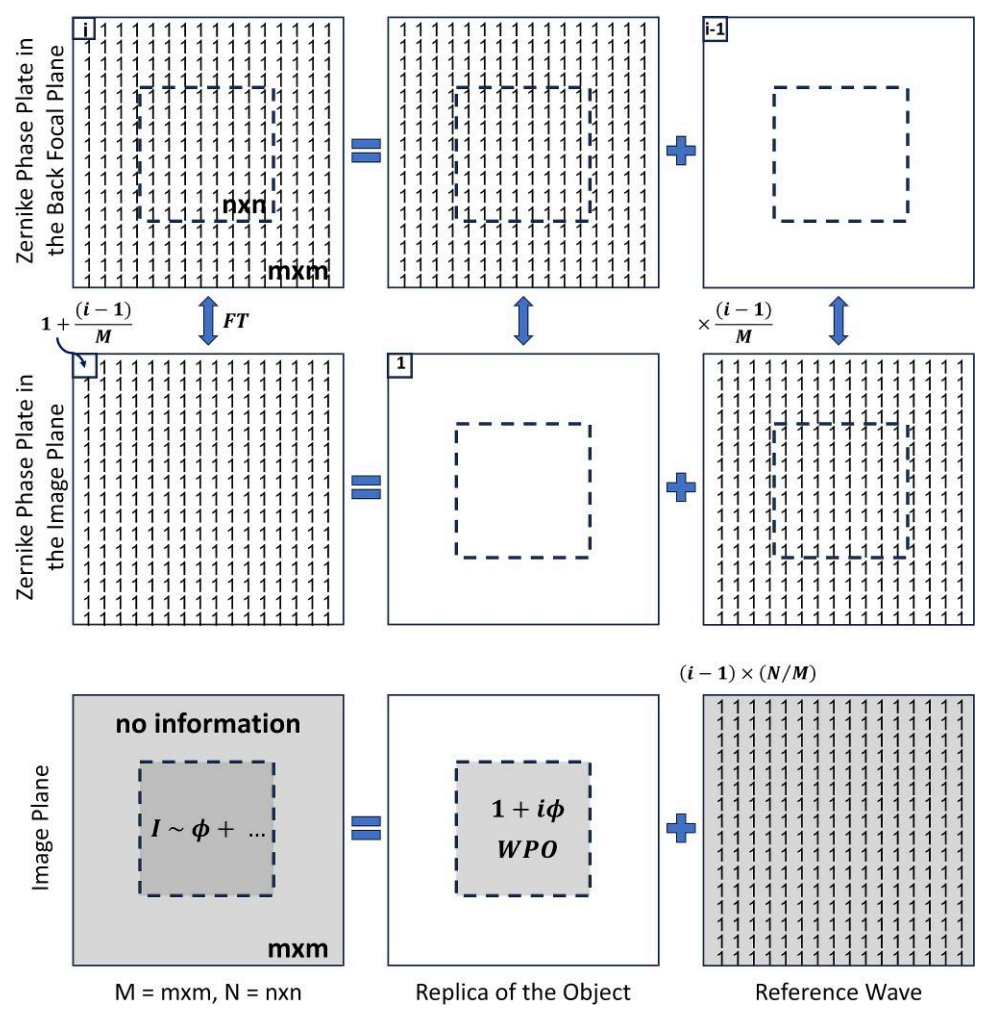


Fig. B.1. Sketch of a numerical 2D implementation of ZPC imaging that avoids aliasing effects that would lead to errors in estimating the quantum efficiency of the ZPC imaging process.

And this looks exactly like we would expect from a ZPP. The standard deviation on the phase now becomes:

$$std(\phi(\mathbf{r})) = \frac{1}{2\sqrt{N_e/M^2}}.$$
 (B.7)

This result is why ZPC is believed to outperform diffraction-based methods, e.g., in (Dwyer & Paganin, 2024).

If, on the other hand, we choose to limit the illumination of the object only to fill $N = n \times n$ pixels, we get a different result with $C = \sqrt{N/M}$, an oversampling factor:

$$\Psi_Z(\mathbf{r}) = O(\mathbf{r}) + C^2(\mathbf{i} - 1)\langle O(\mathbf{r})\rangle \tag{B.8}$$

$$\Psi_Z(\mathbf{r}) = 1 + i\phi(\mathbf{r}) + C^2(i-1)$$
 (B.9)

$$\Psi_Z(\mathbf{r}) = 1 - C^2 + i(C^2 + \phi(\mathbf{r}))$$
 (B.10)

$$I_Z(\mathbf{r}) = 1 - 2C^2 + C^4 + C^4 + 2C^2\phi(\mathbf{r}) + \phi(\mathbf{r})^2$$
 (B.11)

$$I_Z(\mathbf{r}) \approx 1 - 2C^2 + 2C^4 + 2C^2\phi(\mathbf{r}).$$
 (B.12)

We can still derive the phase as follows:

$$\phi(\mathbf{r}) \approx \frac{I_Z - 1 + 2C^2 - 2C^4}{2C^2}$$
 (B.13)

Note that this is subtly different in several ways. If $M \ge 4N$, the action of the averaging kernel now smears the object out over the whole matrix but does not cross the borders of that matrix and, therefore, does not cause aliasing. In physics terms, this means that the average wave, which will be used as a reference beam to reveal the phase, now only comes from the illuminated $n \times n$ patch and not from neighboring sample areas, which, in the case of N = M, are wrongly assumed to be periodic. Even if we can live with the fact that, for the averaging, it does not matter that the sample is perfectly periodic, we are still using electrons from neighboring areas (and they will cause damage there). On top of this, it will spread the averaged reference wave over a wider area in the image plane (here, $m \times m$ but only if $m \ge 2n$). This area is larger than the $n \times n$ illuminated image region of interest. Therefore, a significant fraction of electrons will end up in areas of the image plane where they do not bring information on the illuminated sample area.

We are now in the position to estimate what fraction of the illumination contributes to the ZPC phase signal. Outside and inside the illuminated area, we get an average intensity of:

$$\tilde{I}_{Z,\text{out}} \approx 2C^4$$
 (B.14)

$$\tilde{I}_{Z,\text{in}} \approx 1 - 2C^2 + 2C^4$$
 (B.15)

For an oversampling of C = 1/2, the average intensity is 1 - 2/4 + 1/8 = 5/8 inside and 3/8 on the outside. All intensity is now spread over four times more area in real space than before, and only the central quarter will contain information on the sample phase. That central patch only contains 5/8 of the illumination, but even that 5/8 contributes less than in the aliased (and therefore wrong) ZPC case because the strength of the averaged reference beam is also reduced. For 1D, we have N = n, M = m, and C = 1/2. This would be 1/2 inside and 1/2 outside, leading to half the intensity, which does not contribute to the area of interest.

The standard deviation on the phase now becomes:

$$std(\phi_{Z,aliased}) = \frac{1}{2\sqrt{N_e/N}}$$
 (B.16)

$$\frac{\operatorname{std}(\phi_{Z,2D})}{\operatorname{std}(\phi_{\operatorname{aliased}})} = \frac{\sqrt{1 - 2C^2 + 2C^4}}{C^2}$$
 (B.17)

$$\frac{\operatorname{std}(\phi_{Z,1D})}{\operatorname{std}(\phi_{\operatorname{aliased}})} = \frac{\sqrt{1 - 2C + 2C^2}}{C}.$$
 (B.18)

For the minimal required oversampling of C = 1/2, we get

$$\frac{\text{std}(\phi_{Z,2D})}{\text{std}(\phi_{\text{aliased}})} = \sqrt{10}$$
 (B.19)

$$\frac{\operatorname{std}(\phi_{Z,1D})}{\operatorname{std}(\phi_{\operatorname{aliased}})} = \sqrt{2}.$$
 (B.20)

Identical to the real space derivation as it should be.

APPENDIX C Maximum-Likelihood Model under Poisson Noise

The parameter-dependent part of the log-likelihood for Poisson is given as:

$$l = -\sum_{l}^{N} (I_{\text{exp},l} \ln (I_{\text{model},l}) - I_{\text{model},l}), \tag{C.1}$$

with $I_{\exp,l}$ the experimental observation and $I_{\text{model},l}$, the model prediction is based on a set of detector pixel l parameters. The model is obtained as follows:

$$\Psi_i = A_i e^{i(\phi_i + \alpha_i)} \tag{C.2}$$

$$I_{\text{model},l} = \left| \mathcal{F}_l A_i e^{i(\phi_i + \alpha_i)} \right|^2 \tag{C.3}$$

$$I_{\text{model},l} = \left| \sum_{i} A_{i} e^{i(\phi_{i} + \alpha_{i})} e^{2\pi i \mathbf{r}_{i} \cdot \mathbf{k}_{l}} \right|^{2} = |\tilde{\Psi}_{l}|^{2}. \tag{C.4}$$

We included the optional illumination function $A_i e^{i\alpha_i}$, allowing for both an amplitude and phase-modulated illumination pattern.

Differentiating the log-likelihood from the parameters of the model gives:

$$\frac{\partial l}{\partial \phi_i} = -\sum_{l} \left(\frac{I_{\exp,l}}{I_{\text{model},l}} - 1 \right) \frac{\partial I_{\text{model},l}}{\partial \phi_i}. \tag{C.5}$$

Differentiating the model intensities from the model parameters, we get the:

$$\frac{\partial I_{\text{model},l}}{\partial \phi_i} = -2A_i \mathbf{R} \mathbf{e} \tilde{\Psi} \sin \left(\phi_i + \alpha_i + r_i k_l \right) + 2A_i \mathbf{I} \mathbf{m} \tilde{\Psi} \cos \left(\phi_i + \alpha_i + r_i k_l \right).$$
(C.6)

Suppose we constrain the last phase value ϕ_N to maintain an average phase of zero (the absolute phase has no meaning, and fitters do not like duplicate parameters). In that case, we need to take into account this dependent variable. So, we proceed now with (N-1) independent parameters:

$$\begin{split} \frac{\partial I_{\text{model},l}}{\partial \phi_i} &= -2 \mathbf{Re} \tilde{\Psi}_l [A_i \sin \left(\phi_i + r_i k_l + \alpha_i \right) \\ &- A_N \sin \left(\phi_n + r_n k_l + \alpha_n \right)] \\ &+ 2 \mathbf{Im} \tilde{\Psi}_l [A_i \cos \left(\phi_i + r_i k_l + \alpha_i \right) \\ &- A_N \cos \left(\phi_n + r_n k_l + \alpha_n \right)]. \end{split} \tag{C.7}$$

Using this analytical derivative as a Jacobian input for the nonlinear fitter significantly speeds up the process and improves convergence. We can now derive the Fisher information matrix:

$$F_{i,j} = -E \left[\frac{\partial^2 l}{\partial \phi_i \partial \phi_j} \right] \tag{C.8}$$

$$\begin{split} &= \sum_{l} \frac{\partial}{\partial \phi_{j}} \left(\frac{I_{\text{exp},l}}{I_{\text{model},l}} - 1 \right) \frac{\partial I_{\text{model},l}}{\partial \phi_{i}} \\ &+ \left(\frac{I_{\text{exp},l}}{I_{\text{model},l}} - 1 \right) \frac{\partial I_{\text{model},l}}{\partial^{2} \phi_{i} \partial \phi_{i}} \end{split} \tag{C.9}$$

$$= -\sum_{i} \frac{1}{I_{\text{model},l}} \frac{\partial I_{\text{model},l}}{\partial \phi_{i}} \frac{\partial I_{\text{model},l}}{\partial \phi_{j}}.$$
 (C.10)

From this, we can obtain the $(N-1) \times (N-1)$ covariance matrix:

$$cov = F^{-1}$$
. (C.11)

From which the diagonal elements represent the CRLB of the variance on the individual phase estimates $\tilde{\phi}_i$. This allows us to write a lower limit for the standard deviation on the estimated parameters as:

$$\sigma_{\rm ML} \ge \sqrt{\frac{{
m Tr}({
m cov})}{N-1}}$$
 (C.12)